PHILOSOPHICAL TRANSACTIONS A

royalsocietypublishing.org/journal/rsta

Opinion piece

Cite this article: Ashfold MNR, Kim SK. 2022 Non-Born–Oppenheimer effects in molecular photochemistry: an experimental perspective. *Phil. Trans. R. Soc. A* **380**: 20200376. https://doi.org/10.1098/rsta.2020.0376

Received: 2 June 2021
Accepted: 28 June 2021

One contribution of 11 to a theme issue 'Chemistry without the Born–Oppenheimer approximation'.

Subject Areas:
photochemistry, chemical physics

Keywords:
photochemistry, excited states, conical intersections, non-radiative decay, Born–Oppenheimer approximation

Author for correspondence:
Michael N. R. Ashfold
e-mail: mike.ashfold@bristol.ac.uk

Non-Born–Oppenheimer effects in molecular photochemistry: an experimental perspective

Michael N. R. Ashfold[1] and Sang Kyu Kim[2]

[1]School of Chemistry, University of Bristol, Bristol BS8 1TS, UK
[2]Department of Chemistry, KAIST, Daejeon 34141, Republic of Korea

MNRA, 0000-0001-5762-7048; SKK, 0000-0003-4803-1327

Non-adiabatic couplings between Born–Oppenheimer (BO)-derived potential energy surfaces are now recognized as pivotal in describing the non-radiative decay of electronically excited molecules following photon absorption. This opinion piece illustrates how non-BO effects provide photostability to many biomolecules when exposed to ultraviolet radiation, yet in many other cases are key to facilitating 'reactive' outcomes like isomerization and bond fission. The examples are presented in order of decreasing molecular complexity, spanning studies of organic sunscreen molecules in solution, through two families of heteroatom containing aromatic molecules and culminating with studies of isolated gas phase H_2O molecules that afford some of the most detailed insights yet available into the cascade of non-adiabatic couplings that enable the evolution from photoexcited molecule to eventual products.

This article is part of the theme issue 'Chemistry without the Born–Oppenheimer approximation'.

1. Introduction

The Born–Oppenheimer (BO) approximation recognizes that the electrons in a molecule are very much lighter than the nuclei. Thus, the electrons can move much faster and can be thought to follow the motion of the heavier nuclei adiabatically, whereas the nuclear motions are best viewed as being guided by the average potential energy surface (PES) determined by the electrons. This assumption, that it is permissible to consider the motions of the constituent electrons and nuclei in a molecule

THE ROYAL SOCIETY PUBLISHING

separately, has been a cornerstone of molecular chemistry and physics for almost a century, and the concept of adiabatic PESs defined by the BO approximation is central to current descriptions of molecular spectroscopy and reaction dynamics. Limitations to the picture have also long been recognized, however, and non-adiabatic processes (i.e. processes wherein nuclear motions enable coupling between PESs) should become important in regions of configuration space where two (or more) PESs approach one another in energy. Such regions of degeneracy (or near-degeneracy)—termed conical intersections (CIs)—between PESs are now recognized as being ubiquitous in polyatomic systems; non-adiabatic coupling in such regions of configuration space provides the route by which population is 'funnelled' between multi-dimensional PESs and enables most excited state photophysics, photochemistry and photobiology.

The recent literature contains many excellent texts that summarize our evolving understanding of the key roles of CIs in facilitating ultrafast radiationless processes in molecules [1–11]. Articles in this theme issue anticipate a future where such processes will increasingly be visualized without recourse to the BO approximation and the evolution of photoexcited reactant molecules, for example, may be discussed—in an informative and transparent manner—without recourse to constructing adiabatic PESs and then invoking non-adiabatic couplings to explain the observed dynamics. This opinion piece highlights four recent sets of experimental studies chosen to illustrate consequences of non-BO effects in molecular photochemistry. The chosen examples reflect particular interests of the authors, but the narrative looks to emphasize that the revealed photophysics extrapolates to wider families of molecular systems. The polyatomic systems in each case (i) are sufficiently 'small' to allow consideration of individual nuclear motions and (ii) become progressively smaller as the narrative develops and the quantum state specificity of the non-BO dynamics are revealed more clearly.

2. Photostability: non-radiative relaxation in organic filter molecules

Biological systems are reliant on radiation from the Sun to provide the light, warmth and energy required to sustain life. Excessive exposure to solar ultraviolet (UV) radiation can have adverse consequences, however, and it has been suggested [12] that many biomolecules may have been selected—in part at least—because of the efficiency with which they absorb UV photons and, following photoexcitation, the fidelity with which they return non-radiatively to the ground (S_0) state. The DNA/RNA bases (adenine, cytosine, guanine, thymine and uracil), for example, all show strong $\pi^* \leftarrow \pi$ absorptions centred at wavelengths $\lambda \sim 260$ nm [13]. Photoexcitation at these wavelengths could induce photoreactions and harmful structural changes, yet these bases (and the base pairs) display well-documented photostability. This resistance to photodamage is attributable to efficient, ultrafast non-radiative (and non-reactive) relaxation of the photoexcited molecules back to the S_0 state. Femtosecond time-resolved studies of the isolated bases—in the gas phase and in solution—return excitation energy and environment dependent excited state lifetimes but, in all cases, the lifetimes are short. Non-radiative transfer to the S_0 state in the isolated bases typically occurs on a (sub)picosecond time scale [14–17]. *Ab initio* electronic structure calculations [18,19] reveal the importance of low energy CIs between the excited ($^1\pi\pi^*$) and S_0 state PESs along out-of-plane deformation (ring puckering) coordinates in promoting efficient excited state decay in the isolated nucleobases and additional non-radiative decay (e.g. excited state charge transfer and proton coupled electron transfer) pathways in the polynucleotides.

Sunscreen molecules are another important class of UV-absorbing species. The photophysics of eumelanin, for example, a heterogeneous UV-absorbing pigment composed of cross-linked 5,6-dihydroxyindole (DHI) and 5,6-dihydroxyindole-2-carboxylic acid (DHICA) based polymers and the most abundant melanin in mammalian skin, have been much investigated—experimentally and by theory [20–22]. CI-mediated excited state decay pathways following UV excitation have been identified in the DHI and DHICA monomers [23,24] and small oligomers [25] but many questions remain regarding the photoprotection attributed to these building blocks—particularly

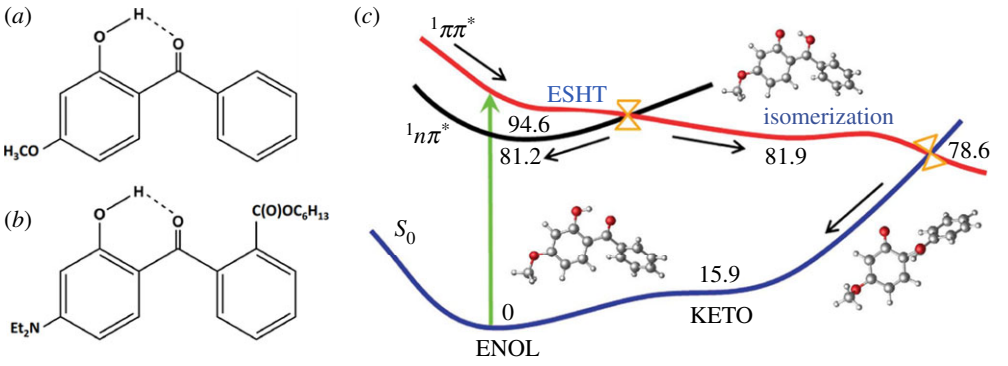

Figure 1. Molecular structures of (*a*) oxybenzone and (*b*) DHHB in its *enol*-form along with (*c*) a schematic depicting the non-radiative decay mechanism following $\pi^* \leftarrow \pi$ excitation of oxybenzone. The $^1\pi\pi^*/^1n\pi^*$ and $^1\pi\pi^*/S_0$ CIs are indicated in orange and the energies are in kcal mol^{-1}. (Adapted from [26], with the permission of AIP Publishing.). (Online version in colour.)

given the identification of an efficient (aqueous) solvent-mediated excited state decay mechanism involving proton coupled electron transfer within and between DHICA oligomers [21].

Organic filters included in commercial sunscreen formulations are more amenable to fundamental study. Oxybenzone (figure 1*a*), for example, is a small, conjugated molecule that exhibits a broad UV absorption profile across the wavelength range $270 \leq \lambda \leq 350$ nm. A combination of ultrafast (femtosecond) transient electronic and vibrational absorption spectroscopy measurements [27,28], at various excitation wavelengths within this range, in solution in cyclohexane and in methanol, and theory (static electronic structure calculations [29] and 'on-the-fly' trajectory surface-hopping dynamics simulations [26]) have led to the non-adiabatic relaxation mechanism summarized in figure 1*c*. Oxybenzone exists predominantly in the *enol*-configuration in its S_0 state. UV excitation populates the strongly absorbing $^1\pi\pi^*$ state, which rapidly relaxes towards its minimum energy *keto*-configuration (i.e. an excited state H atom transfer (ESHT) process, encouraged by the pre-existing intramolecular hydrogen-bond) and onwards towards the CI with the S_0 state at non-planar geometries (one ring twists relative to the other about the central aliphatic C–C bond). A reverse H atom transfer process on the S_0 PES and vibrational energy transfer to the surrounding solvent results in efficient reformation of the original *enol*-isomer with a (solvent dependent) time constant. As shown in figure 1*c*, some of the photoexcited $^1\pi\pi^*$ molecules can evolve via an optically dark $^1n\pi^*$ state (by coupling at the $^1\pi\pi^*/^1n\pi^*$ CI) which has the effect of delaying, but not preventing, their eventual sampling of the $^1\pi\pi^*/S_0$ CI and return to the S_0 PES.

Diethylamino hydroxybenzoyl hexyl benzoate (DHHB) is another UV-absorber used in commercial sunscreens. As figure 1*b* shows, DHHB has a similar core structure to oxybenzone. However, replacing the methoxy- (CH_3O-) group in oxybenzone by an amino group lowers the $\pi^* \leftarrow \pi$ excitation energy and the presence of the ester group on the other aromatic ring helps facilitate charge transfer in the excited state. Like oxybenzone, the minimum energy geometry of DHHB in its S_0 state is the *enol*-tautomer, and the results of recent transient absorption studies following near UV excitation to the first excited $^1\pi\pi^*$ state of DHHB in a non-polar solvent like cyclohexane are consistent with rapid ESHT from the *enol*- to *keto*-tautomer and non-adiabatic coupling back to the S_0 state [30]. But this ESHT process was shown to be inhibited in polar solvents, that can disrupt the intramolecular H-bond. Complementary time dependent density functional theory (TD-DFT) calculations suggest that this could enhance the relative probability of a rival non-adiabatic coupling pathway via a $^1\pi\pi^*/S_0$ CI accessed by torsion about a central C−C bond in the *enol*-tautomer. Other weak, long lived absorptions identified in the study were attributed to minor yields of *enol*-tautomers in the lowest triplet (T_1) state and of an isomeric photoproduct—probably the *trans-enol* tautomer of DHHB in its S_0 state. Addition of octocrylene

(another common ingredient in commercial sunscreen formulations) was found to effectively quench the T_1-*enol* population [30].

These examples illustrate the importance of strongly absorbing, optically 'bright' (typically $^1\pi\pi^*$) states in enabling the initial excitation and the pivotal role of CIs in funnelling population from this excited state, via whatever are the most efficient non-radiative decay pathways, back to the ground state—i.e. in minimizing photodamage. In so doing, the (electronic) energy introduced by photon absorption is efficiently transformed into nuclear (vibrational) motion which, in any condensed phase environment, will rapidly dissipate as heating of the local environment. Non-adiabatic coupling at CIs is also pivotal in most photoinduced *reactions*, however, as illustrated by the remaining three examples.

3. Photoinduced ring opening

Photoinduced isomerizations lie at the heart of many chemical processes [31]. The proposed *trans-enol* tautomer of DHHB in §2 was an (unwanted) photoisomerization product, arising via a rather modest structural change (the reorientation of one part of the molecule relative to another). The structural changes in photoinduced ring-opening reactions, in contrast, are dramatic. One (or more) bonds break, and others may need to break and form, *en route* to the eventual acyclic products. Spyropyrans, for example, have attracted massive interest as molecular switches. Photoexcitation at appropriate UV wavelengths can induce ring opening, yielding a merocyanine, from which the original spyropyran can be recovered by photoexciting at an alternative (visible) wavelength [32]. From a fundamental perspective, the UV photoinduced ring opening of 1,3-cyclohexadiene to 1,3,5-hexatriene [33] has served as a popular model system both for theory (that rationalizes the excited state decay in terms of motion via successive CIs [34]) and for validating emerging probe techniques (e.g. time-resolved photoelectron spectroscopy (TR-PES) [35,36], transient X-ray absorption [37] and X-ray [38,39] and electron [40] diffraction methods) in ultrafast gas phase laser induced pump-probe studies.

Here, we highlight results for the photoinduced ring opening of the prototypical five-membered heterocyclic α-carbonyl compound, 2(5H)-thiophenone, shown in figure 2. Infrared (IR) absorption measurements following UV irradiation of this molecule isolated in an inert argon matrix showed formation of thioaldehyde-ketene products, explicable in terms of photoinduced C–S bond cleavage [42]. Ultrafast transient IR spectroscopy studies following 267 nm photoexcitation of 2(5H)-thiophenone dissolved in acetonitrile confirmed that ring opening occurred on a sub-picosecond timescale, showed that the ring-opened ketene products were formed highly vibrationally excited and found that under these solution-phase conditions approximately 60% of the photoexcited molecules ultimately reformed the cyclic parent [43].

Collision-free, ultrafast studies of the photoinduced ring opening in 2(5H)-thiophenone were reported in 2020 [41]. These used ultrashort pulses of extreme ultraviolet (XUV) light to measure photoelectron spectra at many user-selected time delays, Δt, following 267 nm photoexcitation with a sub-100 fs instrumental time resolution. The experiments were complemented by high level *ab initio* electronic structure and molecular dynamics (MD) simulations for both the excited and ground state molecules. Together, these provide uniquely detailed insights into both the electronic and nuclear dynamics. The false colour plot of electron binding energy (BE) versus pump-probe time delay (figure 2*a*) shows formation and rapid decay of excited state population with BEs in the range 5–8 eV and formation of one or more long-lived products (with BE ~ 9 eV). The accompanying modelling confirms that, following UV excitation to the S_2 state, ballistic C–S bond extension drives the initial ring opening (and biradical formation) and non-adiabatic coupling at CIs with the optically 'dark' S_1 state and then with the S_0 state (figure 2*b*), all within 350 fs. Theory (*ab initio* MD) also allows clear visualization of the subsequent rich dynamics of the highly vibrationally excited S_0 molecules—involving H atom migration, the formation of (and interconversion between) different ring-opened ketene isomers and the reformed cyclic parent structure (all of which contribute to the experimentally observed long lived product signal with BE ~ 9 eV), and eventual loss of CO fragments over a much longer timescale [41].

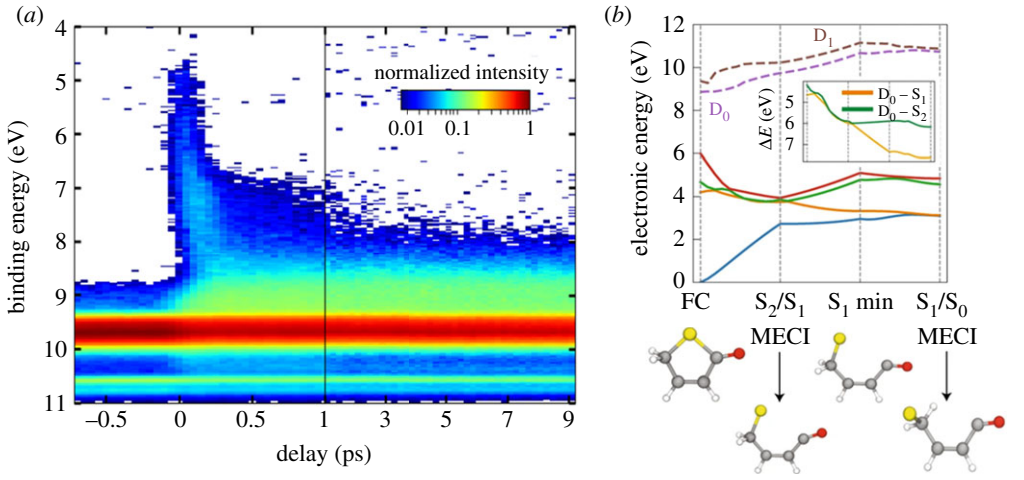

Figure 2. (*a*) Measured photoelectron yield following 267 nm photoexcitation of a jet-cooled sample of 2(5H)-thiophenone displayed as a false colour plot as functions of binding energy (BE) and time delay (Δt) between the 267 nm pump and XUV probe pulses. (*b*) PESs for the first four singlet electronic states of neutral 2(5H)-thiophenone (S_0 through S_3, solid lines) and the lowest two doublet states of the parent cation (D_0 and D_1, dashed lines) computed using a linear interpolation in internal coordinates (LIIC) between different critical geometries—corresponding to the minimum energies of the ground and first excited states (labelled FC and S_1 min, respectively) and the S_2/S_1 and S_1/S_0 minimum energy conical intersections (MECIs), indicated with dashed vertical lines. These structures are shown below, using yellow, red, grey and white to represent, respectively, sulfur, oxygen, carbon and hydrogen atoms. The inset shows the electronic energy gap ΔE between the D_0 state of the cation and the S_2 and S_1 singlet states for each point along the LIIC pathway, which guided interpretation of the time-resolved photoelectron data shown in (*a*). (Adapted from [41]). (Online version in colour.)

These studies of 2(5H)-thiophenone serve to highlight that the same primary photophysics will often lead to different, phase-dependent outcomes. Though the early time dynamics in photoexcited solute molecules in a weakly interacting solvent (or matrix) are likely to be similar to that prevailing in the gas phase, the later time dynamics (e.g. after non-adiabatic coupling back to the S_0 state in the case of 2(5H)-thiophenone) are likely to be very different. In the absence of collisions, the highly vibrationally S_0 molecules can isomerize, dissociate, etc. as described above, whereas in solution this internal energy will dissipate rapidly (typically on a picosecond timescale) through interaction with the surrounding solvent molecules and the solute reactivity will be quenched. Interactions with solvent molecules also cause spectral broadening, which explains the preference for gas phase studies when seeking to explore ways in which parent vibrational (and even rotational) motions influence non-adiabatic coupling between PESs—as illustrated in the remaining two examples.

4. Photoinduced O–H bond fission in phenols. Vibronic state selectivity

Phenol is the chromophore of the amino acid tyrosine, which plays a key role in catalysis facilitated by many enzymes, including photosystem II, the water oxidizing protein complex. $\pi^* \leftarrow \pi$ excitation of phenol at $\lambda \sim 270$ nm populates a (diabatically bound) S_1 state. But, as shown by the one-dimensional potential energy cuts in figure 3*a*, this $^1\pi\pi^*$ state exhibits a conical intersection (CI-1) with a (repulsive) $^1\pi\sigma^*$ state when planar, at extended O–H bond lengths ($R_{O–H}$), with the result that phenol molecules in their S_1 state can predissociate by tunnelling through the potential barrier under CI-1. As figure 3*a* also shows, the dissociating molecules sample a second CI (CI-2, between the diabatic $^1\pi\sigma^*$ and S_0 PESs) at longer $R_{O–H}$, at which the branching between the ground ($\tilde{X}$) and excited ($\tilde{A}$) states of the phenoxyl (PhO) radical product is established [44]. The lifetimes of gas phase phenol molecules excited to the S_1 state

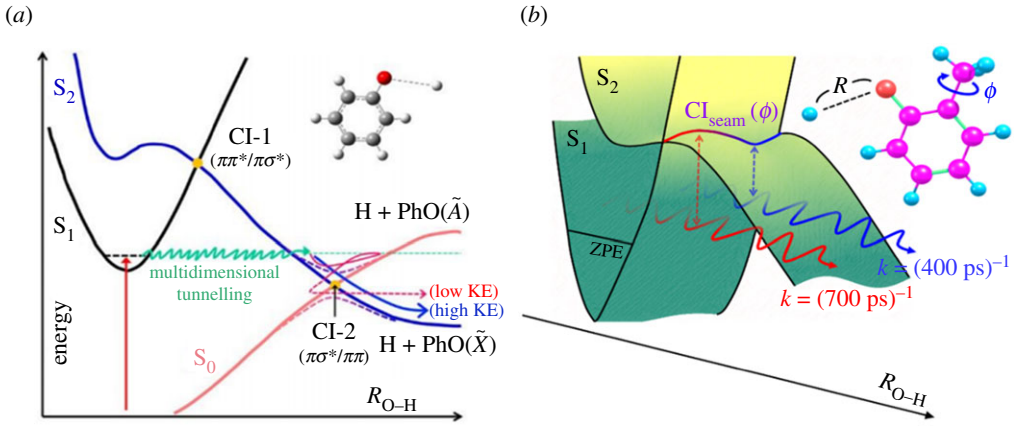

Figure 3. Sections through the S_1 and S_2 PESs relevant to H atom detachment following photoexcitation to S_1, low v′-levels of (*a*) phenol and (*b*) *trans-o*-cresol. The one-dimensional cuts shown in (*a*) illustrate the barrier to tunnelling under CI-1 and the conical intersection CI-2, between the diabatic $^1\pi\sigma^*$ and S_0 PESs, at longer R_{O-H}. The tunnelling process (and the detailed topography of the barrier under CI-1) is inherently multi-dimensional, however, and can be shaped by nuclear distortions in any of the other ($3N - 8$) seam coordinates at CI-1, as illustrated by the two-dimensional PESs for *trans-o*-cresol displayed (as functions of R_{O-H} and the CH_3 torsional angle, ϕ) in (*b*). (Online version in colour.)

are largely determined by the rate of H atom detachment (by tunnelling), though rival non-radiative transitions may also contribute [45–48]. These decay rates are sufficiently slow that the parent S_1–S_0 absorption spectrum shows resolved (ro)vibronic structure, which allows study of how the fragmentation dynamics vary with parent vibrational (v′) level. Henceforth, we focus on the decay of S_1, low v′-levels of phenol which, on energetic grounds, can only dissociate to $H + PhO(\tilde{X})$ products. These radical products are formed in very specific sub-sets of the vibrational levels [49], for reasons that remain a topic of active debate [50,51].

Here, we focus on the v′-dependence of the phenol(S_1) state predissociation rate. Picosecond time-resolved pump-probe studies following excitation to many different phenol S_1, v′-levels (monitoring both the decay of photoexcited parent population and the build-up of H atom products) highlight the limitations of picturing O–H bond fission simply as tunnelling through a one-dimensional barrier along R_{O-H} and assuming that nuclear motions in all orthogonal coordinates are immaterial [47,48]. The tunnelling barrier arises from multi-dimensional curve crossings between excited states, and the tunnelling dynamics are unavoidably complex and multi-dimensional.

Figure 4*a* shows a resonance enhanced two-photon ionization (R2PI) spectrum recorded using one (picosecond duration) laser pulse to excite to selected S_1, v′-levels of a jet-cooled sample of gas phase phenol molecules and a second probe pulse to ionize these excited molecules after a time delay Δt. The spectrum shows resolved vibronic structure and the S_1 decay rates (figure 4*b*) are v′-dependent [48]. The lifetime measured when exciting to the S_1 origin (i.e. $v' = 0$ level) is $\tau \sim 2.3$ ns (figure 4*c*). Lifetimes derived from transients measured when exciting S_1, v′-levels with vibrational energies $E' < 1200\,cm^{-1}$ reveal a strong mode-dependence as illustrated in figure 4*d–h*. For example, $\tau \sim 1.9$ ns when exciting to the $v'_{11} = 2$ (henceforth 11^2) level at $E' = 324\,cm^{-1}$, increases to $\tau \sim 2.9$ ns when $E' = 374\,cm^{-1}$ ($16a^2$), is shorter ($\tau \sim 1.1$ ns) at $E' = 523\,cm^{-1}$ ($6b^1$) and longer again ($\tau \sim 2.1$ ns) at $E' = 975\,cm^{-1}$ ($9a^1$). The fluctuations are less dramatic once $E' > 1200\,cm^{-1}$ and the S_1 lifetime converges to $\tau \approx 800$ ps at $E' \sim 3600\,cm^{-1}$ [48].

These predissociation rates are much slower than typical rates of intramolecular vibrational redistribution (IVR), yet the observation of mode-dependent tunnelling rates clearly shows that the 'bright' (i.e. Franck–Condon favoured) vibronic modes excited in the $0 < E' < 1200\,cm^{-1}$ range maintain distinctive characters during the dissociation. We also note the propensity for

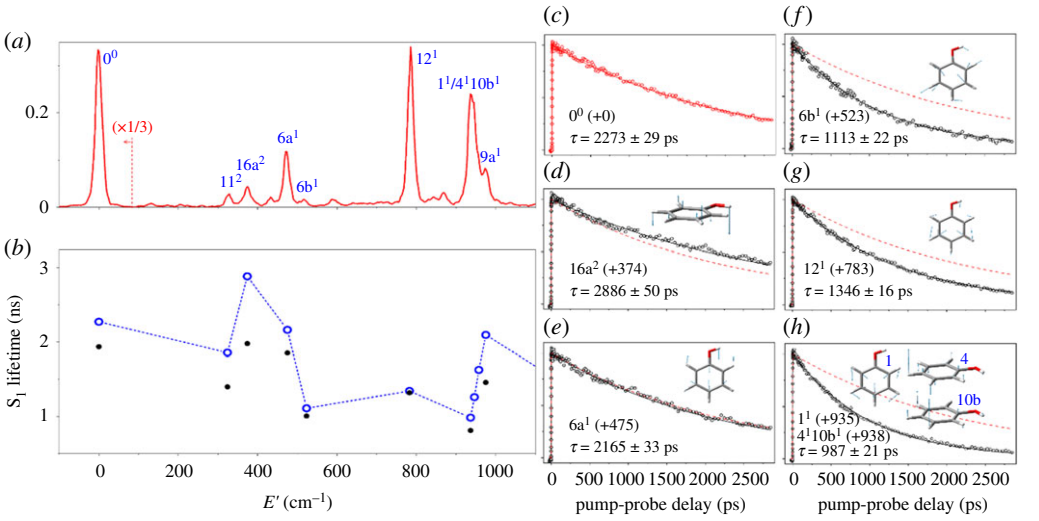

Figure 4. State-specific predissociation rates of phenol(S_1, v′) molecules. (*a*) Picosecond (1 + 1′) R2PI spectrum of a jet-cooled phenol sample with the S_1 mode assignments. The horizontal axis is E', the vibrational energy of the S_1 molecule defined relative to the zero-point energy. (*b*) S_1, v′-level lifetimes derived by fitting to state-selected parent ($C_6H_5OH^+$ (open circles)) and fragment (H^+ (filled circles)) signals measured as a function of pump-probe time delay, Δt. (*c*)–(*h*) show ps time-resolved parent transients following excitation of various S_1, v′ levels with the associated E' value (in cm^{-1}) shown in parentheses. Also included in (*d*)–(*h*) are depictions of the relevant excited state normal mode displacement vectors and the transient measured when exciting the S_1 zero-point level (shown as a thin dashed red line) to highlight the striking mode-dependent differences in decay rate. (Adapted from [48]). (Online version in colour.)

populating certain vibrational modes of the PhO($\tilde{X}$) products, e.g. the out-of-plane ring puckering mode 16a [49], yet the tunnelling rate when exciting the corresponding 16a mode in the S_1 parent molecule is actually slower than when exciting to the S_1, v′ = 0 level [48]. This suggests that the 16a motion is indeed strongly associated with the tunnelling coordinate, in a way that retards the tunnelling process yet induces the associated nuclear motions in the PhO($\tilde{X}$) radical product. The dynamic behaviours revealed in figure 4 imply that the most probable tunnelling paths from different S_1, v′ levels sample different regions of configuration space, and serve to re-emphasize the multi-dimensional nature of the tunnelling dynamics. The nuclear configurations spanned by these different vibronic modes of phenol(S_1) are so wide-ranging, however, that any serious attempt to unravel the mechanisms by which they couple with the tunnelling coordinate would require far more detailed and accurate multi-dimensional PESs for both the S_1 and S_2 PESs, and their non-adiabatic couplings, than are currently available.

Time-resolved R2PI studies of the predissociation of selected S_1 vibronic levels of *ortho-(o-)*cresol (2-methylphenol) provide rather clearer insights [52]. Intuitively, one might have anticipated that replacing one ring-centred H atom in phenol by a methyl group would have little effect on the characteristics of the excited electronic states or the tunnelling dynamics [52–54]. In practice, however, as figure 5 shows, the effects are quite striking. *o*-cresol exists in *trans*- and *cis*-conformers (distinguished by whether the O–H bond points away from or towards the adjacent CH_3 group, respectively), which show different decay (tunnelling) rates [52]. The parent ion transient of *trans-o*-cresol obtained when exciting its S_1, v′ = 0 level returns a lifetime $\tau = 697$ ps (i.e. less than a third that found for bare phenol), while similar measurements exciting the S_1–S_0 origin band of the *cis*-conformer return a biexponential transient signal with an initial decay characterized by $\tau \sim 1.8$ ns. (The biexponential behaviour may indicate some sampling of partially trapped S_1 molecules, and/or of molecules in the T_1 state, or even of vibrationally 'hot' S_0 molecules, and remains an issue requiring further study). The $S_1 - S_0$ spectra of the two

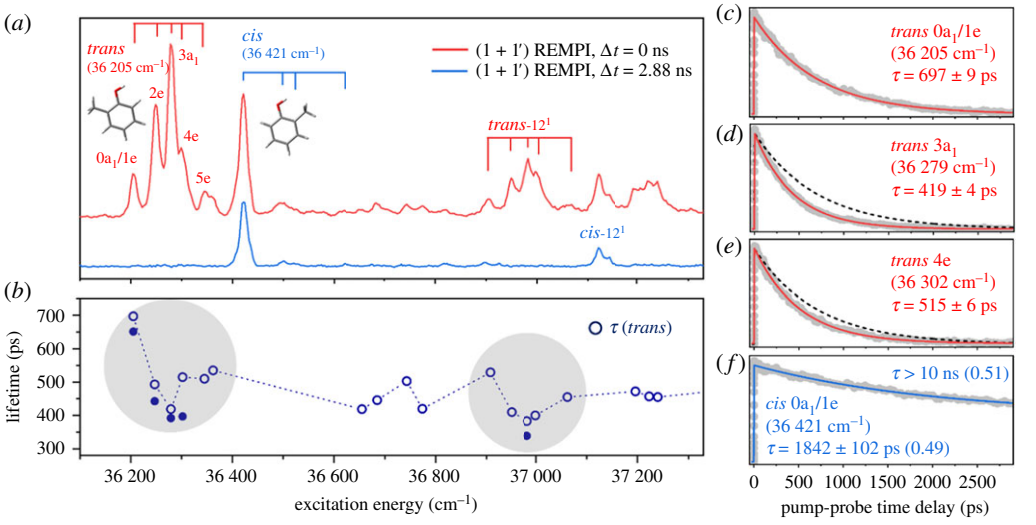

Figure 5. Conformer-specific S_1–S_0 vibronic transitions and S_1 lifetimes of *o*-cresol. (*a*) Picosecond (1 + 1′) R2PI spectra of *o*-cresol taken at $\Delta t = 0$ (red) and 2.88 ns (blue). The CH_3 torsional progression bands are denoted by the combs for the *trans* (red) or *cis* (blue) conformers. (*b*) Lifetimes of the various S_1, v′-levels determined by fitting to parent ($CH_3C_6H_4OH^+$ (open circles)) and fragment (H^+ (closed circles)) signals. (*c*)–(*f*) Picosecond time-resolved parent transients following excitation of different S_1, v′-levels of *trans*-*o*-cresol (in red) and *cis*-*o*-cresol (blue) at the stated wavenumbers (in parentheses). The dashed black trace in (*d*) and (*e*) repeats the *trans*-*o*-cresol data at the zero-point vibrational level ($0a_1/1e$), to emphasize the level dependent decay rates. The numbers in parentheses after the τ values shown for the *cis*-*o*-cresol data are the respective amplitudes returned by the biexponential fitting of this data. (Adapted from [52]). (Online version in colour.)

conformers are heavily overlapped but, as figure 5*a* shows, features associated with each carrier can be readily distinguished via spectra recorded with different pump-probe time delays. The conformer-specific decay time constants accord with theory, which predicts that the $^1\pi\pi^*/^1\pi\sigma^*$ CI (CI-1) lies at relatively higher energy (and thus that the barrier to H atom detachment will be greater) in the case of *cis*-*o*-cresol [52].

The equilibrium configuration of the CH_3 group changes (from staggered to eclipsed, i.e. with one of the three C–H bonds directed at the O atom) upon S_1–S_0 excitation of *trans*-*o*-cresol, which allows Franck–Condon access to several excited CH_3 internal rotor levels within the S_1 state of this conformer [55]. These span a small range of energies ($0 < E' < 100\,cm^{-1}$) yet, as figure 5 shows, display obviously different decay time constants: $\tau \sim 697$ ps (at the zero-point ($0a_1/1e$) level), declining to $\tau \sim 419$ ps for the $3a_1$ level, then increasing again for the higher energy 4e and 5e levels. Such variations in tunnelling rate over such a small range of energies, associated with a group remote from the breaking bond, are highly unusual. The tunnelling rates measured when exciting other S_1 vibronic levels are all close to $k \sim (500\,ps)^{-1}$ across the energy range $0 < E' < 2000\,cm^{-1}$, suggesting that internal energy in *trans*-*o*-cresol(S_1) modes other than the CH_3 torsion is of little benefit in overcoming and/or altering the barrier to tunnelling.

These findings suggest the applicability of a reduced-dimensional picture of the predissociation of *o*-cresol by tunnelling along $R_{O\text{–}H}$ [52]. Focusing on the *trans*-conformer, the $S_1(^1\pi\pi^*)$ and $S_2(^1\pi\sigma^*)$ states are predicted to have different minimum energy geometries (with the CH_3 group, respectively, eclipsed and staggered). The barrier to internal rotation of the CH_3 group in the S_1 state is significantly smaller than that in the $S_2(^1\pi\sigma^*)$ state. Thus, the torsional potential in the vicinity of CI-1 will be a sinusoidal function with crests and troughs corresponding to, respectively, eclipsed ($\phi = 0°$) and staggered ($\phi = 60°$) conformations (with maximal energies separated by approx. $400\,cm^{-1}$) [52]. Molecules excited to a particular CH_3 rotor level in the S_1 state decay by tunnelling through the barrier along $R_{O\text{–}H}$, the detailed topography of which

is 'dynamically shaped' by the way CI-1 varies along the CH_3 torsional seam coordinate. The observed torsional-level-dependent variations in tunnelling rate can be reproduced well using a two-dimensional model, shown schematically in figure 3*b*, wherein the tunnelling probability is determined by the 'effective' barrier obtained by weighting the calculated barrier to tunnelling ($V(R_{O\text{–}H};\phi)$) by the ϕ-dependence of the probability with which it is sampled (given by the square of the relevant torsional wave function over the full $0 \leq \phi \leq 360°$ range) [52].

Phenols are just one of many families of hydrides that decay by X–H (X = O, S, N, etc.) bond fission after coupling to a dissociative $^1\pi\sigma^*$ PES [44,56–58]. Parent vibronic mode-dependent tunnelling rates and product quantum state population distributions have been reported for several similar systems including catechol [59,60], thiophenol and several *o*-substituted thiophenols [61–63]. In all these cases, excitation of the out-of-plane torsional motion of the OH (or SH) moiety results in an increased tunnelling rate, implying that the effective barrier to tunnelling is reduced by increasing the dihedral angle between the OH (or SH) moiety and the molecular plane—again in accord with theoretical predictions [64–67].

It is important to reiterate that these O–H (or S–H) bond ruptures following excitation to low v′ levels in the S_1 state occur via tunnelling through barriers that are shaped by non-adiabatic interactions between multi-dimensional PESs centred at energies that—particularly in the case of the phenols—are well above that of the tunnelling system. Visualizing and understanding the multi-dimensional facets of such tunnelling processes in these and related systems (e.g. anisoles and thioanisoles [68–71]) remains a formidable challenge—particularly if this requires proper inclusion of the geometric phase effect and the associated constructive and/or destructive interferences of dissociating flux traversing the CI region(s) [72–74]. Extending this photophysical understanding to such molecules in solution presents further challenges: Ultrafast pump (267 nm)—probe studies of phenol in aqueous solution, for example, return similar (nanosecond) decay time constants for forming PhO($\tilde{X}$) photoproducts (along with aquated electrons and protons) [75] but find orders of magnitude faster decay rates when the phenol molecules are located at the air–water interface [76].

5. Photoinduced O–H bond fission in H_2O. Rovibronic state selectivity

Our final examples illustrating the richness and ubiquity of non-BO dynamics are drawn from the extensive studies of excited states of H_2O molecules in the gas phase. H_2O is much the simplest molecular system considered in this review. It is sufficiently light that its photodissociation can be studied with high (rovibrational) quantum state resolution, both in the parent precursor and in any diatomic products. It is an ideal test bed for exploring effects of full (and partial) H/D isotopic substitution and, with just 10 electrons and three vibrational degrees of freedom, it is very amenable to high level quantum calculations.

All electronic excitations from the ground state of H_2O lie at energies greater than 6 eV (i.e. the absorption spectrum lies entirely in the VUV spectral region) [77]. Excitation in the range $150 < \lambda < 190$ nm populates the first excited singlet ($\tilde{A}$) state and results in direct dissociation to yield an H atom and a ground (X) state OH radical with only modest rotational and vibrational excitation [78–81]. The photodissociation of H_2O in its second ($\tilde{B} - \tilde{X}$) absorption band centred at $\lambda \sim 128$ nm, in contrast, has long served as a prototype for exploring and understanding non-adiabatic dynamics in (small) polyatomic molecules [82–88]. Direct dissociation following excitation to the $\tilde{B}$ state yields electronically excited OH(A) products along with an H atom. However, the major products following photoexcitation to this state are H atoms together with OH(X) radicals, which can arise via a range of non-adiabatic pathways. As figure 6 shows, these include non-adiabatic coupling between the $\tilde{B}$ and $\tilde{X}$ state PESs at CIs sampled by extending one O–H bond length ($R_{O\text{–}H}$) and opening the inter-bond angle (∠HOH) to linear H–O–H and O–H–H geometries, and by (Renner–Teller) coupling at the seam of degeneracy between the $\tilde{B}$ and $\tilde{A}$ state PESs at shorter $R_{O\text{–}H}$ [84,85,87,89,90].

Following vertical excitation from the bent ground state equilibrium geometry, the topography of the $\tilde{B}$ state PES ensures rapid opening of ∠HOH in tandem with extension of an O–H bond; the

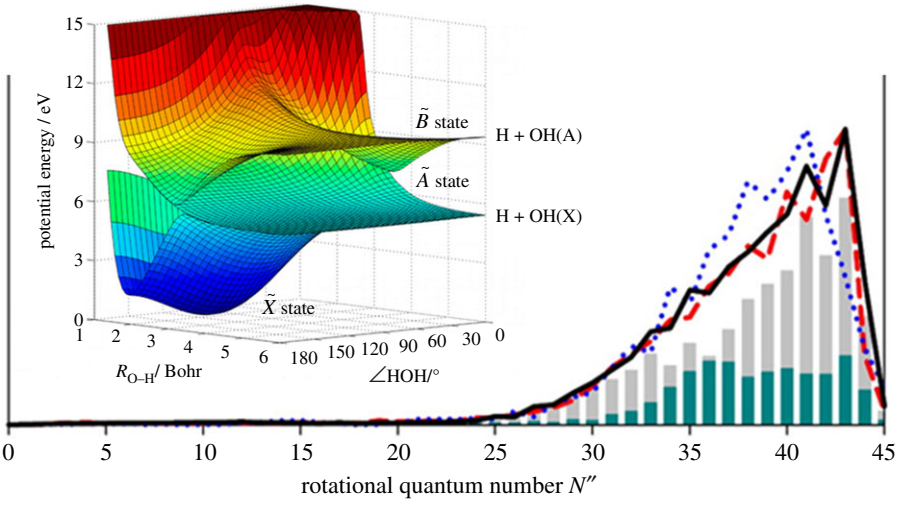

Figure 6. Left: PESs for the $\tilde{B}$, $\tilde{A}$ and $\tilde{X}$ states of H_2O plotted as functions of one O–H bond length, R_{O-H}, and the inter-bond angle, ∠HOH, with the other O–H bond length fixed at the equilibrium value in the ground state ($1.8a_0$), illustrating the CIs at linear H–O–H and O–H–H geometries and the seam of degeneracy between the $\tilde{B}$ and $\tilde{A}$ state PESs at shorter R_{O-H}. Right: Measured (solid black curve) OH(X, v″ = 0) product rotational (*N*″) state population distribution formed upon photoexcitation of a jet-cooled H_2O sample at 128.12 nm, together with the *ab initio* predicted *N*″ distribution (red dashed curve) arising via non-adiabatic coupling at the CI between the $\tilde{B}$ and $\tilde{X}$ PESs at linear H–O–H geometries (shown by the grey bars) and by Renner–Teller coupling between the $\tilde{B}$ and $\tilde{A}$ state PESs (cyan bars). The dotted blue curve shows the *N*″ distribution predicted by an earlier calculation that neglected possible contributions from the Renner–Teller coupling pathway. (Adapted from [87]. Copyright (2013) American Chemical Society). (Online version in colour.)

former motion is the source of the observed massive rotational excitation of the OH(X) products—illustrated in figure 6 for the case of 128.12 nm excitation. Careful analyses of the OH(X) product rotational state population distributions following photoexcitation of H_2O at the Lyman-α wavelength (λ = 121.57 nm, the most intense contributor to the interstellar radiation field) shows a striking odd-even *N*″ intensity alternation. At this higher excitation energy, the angle opening forces are sufficient that some departing H atoms 'orbit' their OH partner sufficiently to access the region of CI between the $\tilde{B}$ and $\tilde{X}$ state PESs at linear O–H–H geometries; wavepacket calculations show that the observed alternation in the product rotational state population distribution is a signature of dynamical interference between pathways that pass through the rival CIs [91–93].

The H_2O absorption spectrum displays many intense resonances at shorter wavelengths, associated with excitations to predissociated Rydberg states [77,94]. The aforementioned excitation at λ = 121.57 nm populates the v′ = 0 level of the $\tilde{D}$ Rydberg state, which predissociates on a timescale that is sufficiently slow that the spectrum of a jet-cooled sample shows lifetime-broadened vibronic (but no resolvable rovibronic) structure. The near-lying $\tilde{C}$ Rydberg state predissociates more slowly, however, and provides an opportunity to excite individual rovibronic transitions within the $\tilde{C} - \tilde{X}$ origin band at λ ∼ 124 nm and find that different rotational levels of the $\tilde{C}$ state predissociate at different rates [95] and give rise to strikingly different H + OH(X/A) rovibrational state population distributions [96]. These differences can be traced to the operation of both homogeneous (i.e. rotation independent) and heterogeneous (rotational level dependent, or Coriolis-induced) predissociation pathways. The efficiency of the latter increases with $\langle J_a^2 \rangle$, i.e. with the expectation value of the square of the rotational angular momentum about the *a*-inertial axis. These rival pathways can be understood in terms of non-adiabatic coupling to the dissociative continua responsible for, respectively, the $\tilde{A} - \tilde{X}$ and $\tilde{B} - \tilde{X}$ absorptions [96].

This example serves to highlight the cascade of non-adiabatic couplings required to enable dissociation to H + OH(X) products: molecules initially excited to the $\tilde{C}$, v′ = 0 level couple to

the $\tilde{A}$ or $\tilde{B}$ state PESs, with relative probabilities that are rotational level—and thus sample temperature—dependent. Those that follow the former pathway yield rotationally 'cold' but vibrationally excited OH(X) products [97], while most of those that undergo Coriolis-coupling to the $\tilde{B}$ state PES undergo a further non-adiabatic coupling to the $\tilde{A}$ or $\tilde{X}$ state PESs—yielding vibrationally 'cold' but highly rotationally excited OH(X) products. Introducing a quantum of bending vibrational excitation results in strikingly isotopologue-dependent fragmentation behaviour which can be understood by recognizing that, in the specific case of H_2O, the $\tilde{C}$, $v_2' = 1$ level is resonant with the $\tilde{D}$, $v' = 0$ level, coupling via which offers another vibronic (i.e. rotational level independent) non-adiabatic pathway to the $\tilde{A}$ state PES and thence to H + OH(X) products [98,99].

Studies of H_2O following photoexcitation at other VUV excitation wavelengths reveal that fragmentation via a succession of non-adiabatic couplings is the norm and one can anticipate that future studies will show that such behaviour extrapolates to the decay of higher excited states of most small molecules. We conclude this section by noting two other examples from within the portfolio of recent studies of H_2O. More than 30% of all the OH(X) fragments formed when H_2O molecules are excited to the $\tilde{D}$ (110) level (i.e. the $\tilde{D}$ state level with quanta in both the symmetric stretch and the bending vibrational modes) at $\lambda \sim 115.2$ nm and decay by non-adiabatic coupling to the $\tilde{B}$ state and thence to the $\tilde{X}$ state PES are 'super-rotors' (i.e. species with rotational energies greater than the O–H bond dissociation energy, D_0(O–H), that exist only by virtue of the centrifugal barrier in the potential energy function associated with the high rotational angular momentum) [100]. The OH(X) fragments formed following excitation to the $\tilde{E}$, $v' = 0$ level at $\lambda \sim 112.8$ nm, in contrast, show an inverted vibrational state population distribution that maximizes at $v'' = 9$ and extends to at least $v'' = 15$ (i.e. to within 600 cm^{-1} of D_0(O–H)). This energy disposal is also attributable to a sequence of non-adiabatic couplings via—in this case—an intermediate state of $^1A_2$ symmetry *en route* to the $\tilde{A}$ state PES. These couplings are enabled by asymmetric stretching motion in regions of configuration space where the respective PESs are near degenerate—i.e. at geometries involving one short and one extended O–H bond length; the OH(X, high v″) products derive from the O–H bond that 'survives' after the final coupling to the $\tilde{A}$ state PES. Atmospheric chemistry modelling indicates that OH(X, high v″) radicals from H_2O photolysis might be detectable in the OH Meinel band dayglow in the upper atmosphere of Earth, and should dominate the corresponding emission from the Martian atmosphere [101].

6. Conclusion and future prospects

Non-adiabatic couplings between BO-derived PESs are now recognized as crucial to describing the funnelling of photoexcited molecules to lower excited states and/or to 'reactive' outcomes like isomerization and bond rupture. This opinion piece has sought to illustrate the key roles of non-BO effects in the photochemistry of four sets of molecules—ranging from affording photostability to many biomolecules to facilitating isomerization and bond fission following UV photoexcitation of many other small molecules. The examples have been introduced in order of decreasing molecular complexity, culminating in the case of gas phase H_2O molecules which afford some of the most detailed insights yet available into the cascade of non-adiabatic couplings that can be involved in the evolution from photoexcited molecule to eventual products, and the range of coupled nuclear/electron motions involved in the evolution.

Most of the descriptions have focused on the systems in their 'simplest' form, i.e. as isolated molecules in the gas phase, though the DHHB example illustrates that the BO PESs of the solute and the non-adiabatic couplings between them may be (in many cases substantially) modified by interaction with solvent molecules. But even under isolated molecule conditions, the PESs can be modified by external fields and we note recent interest in using intense non-resonant (typically near IR) laser fields and the dynamic Stark effect to shift and reshape the field-free BO PESs and the couplings between them. Notable demonstrations include intense IR-field induced changes in the relative yields of ground and spin-orbit excited Br atoms in the near UV photodissociation

of IBr [102] and of ground and spin-orbit excited I atoms in the UV photolysis of CH_3I [103], in the speed distributions of the H atoms resulting from UV photolysis of phenol (implying changes in the vibronic population distribution in the phenoxyl radical partner) [104] and even in the efficiency of the UV-driven isomerization of *cis*- to *trans*-stilbene in solution in cyclohexane [105].

Finally, we briefly speculate on the prospects for 'measuring' non-BO dynamics experimentally. At one level, this is already possible through, for example, the measurement of (spin-orbit) product branching ratios in popular test-bed molecules like IBr [106] or CH_3I [107]—concepts that could surely be extended in the present context to careful, systematic and quantitative measurements of the electronic branching between $PhO(\tilde{A})/PhO(\tilde{X})$ and $PhS(\tilde{A})/PhS(\tilde{X})$ products in the UV photolysis of phenols, anisoles and the thio-analogues. But such measurements reveal the effects of non-BO dynamics, rather than allowing direct visualization of the dynamics prevailing in the immediate vicinity of a CI. IBr and CH_3I have also proven to be popular systems when seeking to probe non-BO dynamics more directly, using ultrafast pump-probe methods to observe the bifurcation of the excited state population (i.e. the evolving wavepacket) in the regions of curve crossing/CI between excited state potentials in these simple halide molecules [108–110]. Even in these very well-studied systems, however, experimental data is typically still validated and interpreted by recourse to the best available theoretical predictions [108,111].

Ultrafast TR-PES methods are also finding increased use in tracking the evolution of photoexcited molecules through CIs—as illustrated here for the case of thiophenone [41]—and (weak) vibronic coherences identified in recent time-resolved X-ray diffraction (TR-XRD) experiments have been interpreted as providing insights into the timing of, and the confined spatial distributions of the valence electrons in, the CI-enabled *cis* → *trans* isomerization of photoexcited azobenzene molecules [112,113]. In all cases, however, interpretation of the experimental data is heavily reliant on complementary high level theoretical modelling, and the unambiguous interpretation of such ultrafast data measured for more complex, higher dimensionality systems, in the absence of supporting high level theory, is likely to remain a substantial challenge.

Data accessibility. This article has no additional data.

Authors' contributions. The authors contributed equally to the preparation and writing of this manuscript. All authors gave final approval for publication and agreed to be held accountable for the work performed therein.

Competing interests. The authors declare no competing interests.

Funding. M.N.R.A. acknowledges recent past funding from the Engineering and Physical Sciences Research Council (EPSRC, EP/L005913). S.K.K. is grateful for financial support from the National Research Foundation of Korea (grant nos. 2018R1A2B3004534 and 2019R1A6A1A10073887).

Acknowledgements. Both authors are grateful to their many respective students and to colleagues around the world for numerous constructive interactions over the years.

References

1. Köppel H, Domcke W, Cederbaum LS. 1984 Multimode molecular-dynamics beyond the Born-Oppenheimer approximation. *Adv. Chem. Phys.* **57**, 59–246. (doi:10.1002/9780470142813)
2. Bernardi F, Olivucci M, Robb MA. 1996 Potential energy surface crossings in organic photochemistry. *Chem. Soc. Rev.* **25**, 321–328. (doi:10.1039/cs9962500321)
3. Butler LJ. 1998 Chemical reaction dynamics beyond the Born-Oppenheimer approximation. *Ann. Rev. Phys. Chem.* **49**, 125–171. (doi:10.1146/annurev.physchem.49.1.125)
4. Ben-Nun M, Quenneville J, Martinez TJ. 2000 Ab initio multiple spawning: photochemistry from first principles quantum molecular dynamics. *J. Phys. Chem. A* **104**, 5161–5175. (doi:10.1021/jp994174i)
5. Worth GA, Cederbaum LS. 2004 Beyond Born-Oppenheimer: molecular dynamics through a conical intersection. *Ann. Rev. Phys. Chem.* **55**, 127–158. (doi:10.1146/annurev.physchem.55.091602.094335)

6. Levine BG, Martinez TJ. 2007 Isomerization through conical intersections. *Ann. Rev. Phys. Chem.* **58**, 613–634. (doi:10.1146/annurev.physchem.57.032905.104612)
7. Domcke W, Yarkony DR, Köppel H. 2011 *Conical intersections: theory, computation and experiment*. Singapore: World Scientific.
8. Matsika S, Krause P. 2011 Nonadiabatic events and conical intersections. *Ann. Rev. Phys. Chem.* **62**, 621–643. (doi:10.1146/annurev-physchem-032210-103450)
9. Domcke W, Yarkony DR. 2012 Role of conical intersections in molecular spectroscopy and photoinduced chemical dynamics. *Ann. Rev. Phys. Chem.* **63**, 325–352. (doi:10.1146/annurev-physchem-032210-103522)
10. Curchod BFE, Martinez TJ. 2018 Ab initio nonadiabatic quantum molecular dynamics. *Chem. Rev.* **118**, 3305–3336. (doi:10.1021/acs.chemrev.7b00423)
11. Crespo-Otero R, Barbatti M. 2018 Recent advances and perspectives on nonadiabatic mixed quantum-classical dynamics. *Chem. Rev.* **118**, 7026–7068. (doi:10.1021/acs.chemrev.7b00577)
12. Boldissar S, de Vries MS. 2018 How nature covers its bases. *Phys. Chem. Chem. Phys.* **20**, 9701–9717. (doi:10.1039/c8cp01236a)
13. Voet D, Gratzer WB, Cox RA, Doty P. 1963 Absorption spectra of nucleotides, polynucleotides, and nucleic acids in the far ultraviolet. *Biopolymers* **1**, 193–208. (doi:10.1002/bip.360010302)
14. Pecourt JML, Peon J, Kohler B. 2001 DNA excited-state dynamics: ultrafast internal conversion and vibrational cooling in a series of nucleosides. *J. Am. Chem. Soc.* **123**, 10 370–10 378. (doi:10.1021/ja0161453)
15. Crespo-Hernandez CE, Cohen B, Hare PM, Kohler B. 2004 Ultrafast excited-state dynamics in nucleic acids. *Chem. Rev.* **104**, 1977–2019. (doi:10.1021/cr0206770)
16. Schreier WJ, Gilch P, Zinth W. 2015 Early events of DNA photodamage. *Ann. Rev. Phys. Chem.* **66**, 497–519. (doi:10.1146/annurev-physchem-040214-121821)
17. Middleton CT, de La Harpe K, Su C, Law YK, Crespo-Hernandez CE, Kohler B. 2009 DNA excited-state dynamics: from single bases to the double helix. *Ann. Rev. Phys. Chem.* **60**, 217–239. (doi:10.1146/annurev.physchem.59.032607.093719)
18. Improta R, Santoro F, Blancafort L. 2016 Quantum mechanical studies on the photophysics and the photochemistry of nucleic acids and nucleobases. *Chem. Rev.* **116**, 3540–3593. (doi:10.1021/acs.chemrev.5b00444)
19. Marchetti B, Karsili TNV, Ashfold MNR, Domcke W. 2016 A 'bottom up', ab initio computational approach to understanding fundamental photophysical processes in nitrogen containing heterocycles, DNA bases and base pairs. *Phys. Chem. Chem. Phys.* **18**, 20 007–20 027. (doi:10.1039/c6cp00165c)
20. Corani A, Huijser A, Gustavsson T, Markovitsi D, Malmqvist PA, Pezzella A, d'Ischia M, Sundström V. 2014 Superior photoprotective motifs and mechanisms in eumelanins uncovered. *J. Am. Chem. Soc.* **136**, 11 626–11 635. (doi:10.1021/ja501499q)
21. Nogueira JJ, Corani A, El Nahhas A, Pezzela A, d'Ischia M, González L, Sundström V. 2017 Sequential proton-coupled electron transfer mediates excited-state deactivation of a eumelanin building block. *J. Phys. Chem. Lett.* **8**, 1004–1008. (doi:10.1021/acs.jpclett.6b03012)
22. Kohl FR, Grieco C, Kohler B. 2020 Ultrafast spectral hole burning reveals the distinct chromophores in eumelanin and their common photoresponse. *Chem. Sci.* **11**, 1248–1259. (doi:10.1039/c9sc04527a)
23. Corani A, Pezzella A, Pascher T, Gustavsson T, Markovitsi D, Huijser A, d'Ischia M, Sundström V. 2013 Excited-state proton-transfer processes of DHICA resolved: from sub-picoseconds to nanoseconds. *J. Phys. Chem. Lett.* **4**, 1383–1388. (doi:10.1021/jz400437q)
24. Ghosh P, Ghosh D. 2019 Non-radiative decay of an eumelanin monomer: to be or not to be planar. *Phys. Chem. Chem. Phys.* **21**, 6635–6642. (doi:10.1039/c9cp00246d)
25. Marchetti B, Karsili TNV. 2016 Theoretical insights into the photo-protective mechanisms of natural biological sunscreens: building blocks of eumelanin and pheomelanin. *Phys. Chem. Chem. Phys.* **18**, 3644–3658. (doi:10.1039/c5cp06767g)
26. Li CX, Guo WW, Xie BB, Cui GL. 2016 Photodynamics of oxybenzone sunscreen: nonadiabatic dynamics simulations. *J. Chem. Phys.* **145**, 074308. (doi:10.1063/1.4961261)
27. Baker LA, Horbury MD, Greenough SE, Coulter PM, Karsili TNV, Roberts GM, Orr-Ewing AJ, Ashfold MNR, Stavros VG. 2015 Probing the ultrafast energy dissipation mechanism

of the sunscreen oxybenzone after UVA irradiation. *J. Phys. Chem. Lett.* **6**, 1363–1368. (doi:10.1021/acs.jpclett.5b00417)
28. Baker LA, Horbury MD, Greenough SE, Ashfold MNR, Stavros VG. 2015 Broadband ultrafast photoprotection by oxybenzone across the UVB and UVC spectral regions. *Photochem. Photobiol. Sci.* **14**, 1814–1820. (doi:10.1039/c5pp00217f)
29. Karsili TNV, Marchetti B, Ashfold MNR, Domcke W. 2014 Ab initio study of potential ultrafast internal conversion routes in oxybenzone, caffeic acid, and ferulic acid: implications for sunscreens. *J. Phys. Chem. A* **118**, 11 999–12 010. (doi:10.1021/jp507282d)
30. Kao MH, Venkatraman RK, Sneha M, Wilton M, Orr-Ewing AJ. 2021 Influence of the solvent environment on the ultrafast relaxation pathways of a sunscreen molecule diethylamino hydroxybenzoyl hexyl benzoate. *J. Phys. Chem. A* **125**, 636–645. (doi:10.1021/acs.jpca.0c10313)
31. Kumpulainen T, Lang B, Rosspeinter A, Vauthey E. 2017 Ultrafast elementary photochemical processes of organic molecules in liquid solution. *Chem. Rev.* **117**, 10 826–10 939. (doi:10.1021/acs.chemrev.6b00491)
32. Klajn R. 2014 Spyropyran-based dynamic materials. *Chem. Soc. Rev.* **43**, 148–184. (doi:10.1039/c3cs60181a)
33. Deb S, Weber PM. 2011 The ultrafast pathway of photon-induced electrocyclic ring-opening reactions: the case of 1,3-cyclohexadiene. *Ann. Rev. Phys. Chem.* **62**, 19–39. (doi:10.1146/annurev.physchem.012809.103350)
34. Polyak I, Hutton L, Crespo-Otero R, Barbatti M, Knowles PJ. 2019 Ultrafast photoinduced dynamics of 1,3-cyclohexadiene using XMS-CASPT2 surface hopping. *J. Chem. Theory Comp.* **15**, 3929–3940. (doi:10.1021/acs.jctc.9b00396)
35. Rudakov F, Weber PM. 2009 Ground state recovery and molecular structure upon ultrafast transition through conical intersections in cyclic dienes. *Chem. Phys. Lett.* **470**, 187–190. (doi:10.1016/j.cplett.2009.01.058)
36. Adachi S, Sato M, Suzuki T. 2015 Direct observation of ground-state product formation in a 1,3-cyclohexadiene ring-opening reaction. *J. Phys. Chem. Lett.* **6**, 343–346. (doi:10.1021/jz502487r)
37. Attar AR, Bhattacherjee A, Pemmaraju CD, Schnorr K, Closser KD, Prendergast D, Leone SR. 2017 Femtosecond X-ray spectroscopy of an electrocyclic ring-opening reaction. *Science* **356**, 54–58. (doi:10.1126/science.aaj2198)
38. Minitti MP *et al.* 2015 Imaging molecular motion: femtosecond X-ray scattering of the ring opening in 1,3-cyclohexadiene. *Phys. Rev. Lett.* **114**, 255501. (doi:10.1103/PhysRevLett.114.255501)
39. Ruddock JM *et al.* 2019 A deep UV trigger for ground-state ring-opening dynamics of 1,3-cyclohexadiene. *Sci. Adv.* **5**, eaax6625. (doi:10.1126/sciadv.aax6625)
40. Wolf TJA *et al.* 2019 The photochemical ring-opening of 1,3-cyclohexadiene imaged by ultrafast electron diffraction. *Nat. Chem.* **11**, 504–509. (doi:10.1038/s41557-019-0252-7)
41. Pathak S *et al.* 2020 Tracking the ultraviolet-induced photochemistry of thiophenone during and after ultrafast ring opening. *Nat. Chem.* **12**, 795–800. (doi:10.1038/s41557-020-0507-3)
42. Breda S, Reva I, Fausto R. 2009 UV-induced unimolecular photochemistry of 2(5H)-thiophenone isolated low temperature inert matrices. *Vib. Spectrosc.* **50**, 57–67. (doi:10.1016/j.vibspec.2008.07.015)
43. Murdock D, Harris SJ, Luke J, Grubb MP, Orr-Ewing AJ, Ashfold MNR. 2014 Transient UV pump-IR probe investigation of heterocyclic ring-opening dynamics in the solution phase: the role played by $n\sigma^*$ states in the photoinduced reactions of thiophenone and furanone. *Phys. Chem. Chem. Phys.* **16**, 21 271–21 279. (doi:10.1039/c4cp03653k)
44. Sobolewski AL, Domcke W, Dedonder-Lardeux C, Jouvet C. 2002 Excited-state hydrogen attachment and hydrogen transfer driven by repulsive $^1\pi\sigma^*$ states: a new paradigm for nonradiative decay in aromatic biomolecules. *Phys. Chem. Chem. Phys.* **4**, 1093–1100. (doi:10.1039/b110941n)
45. Tseng CM, Lee YT, Ni CK. 2004 H atom elimination from the $\pi\sigma^*$ state in the photodissociation of phenol. *J. Chem. Phys.* **121**, 2459–2461. (doi:10.1063/1.1781153)
46. Roberts GM, Chatterley AS, Young JD, Stavros VG. 2012 Direct observation of hydrogen tunneling dynamics in photoexcited phenol. *J. Phys. Chem. Lett.* **3**, 348–352. (doi:10.1021/jz2016318)

47. Lai HY, Jhang WR, Tseng CM. 2018 Communication: mode-dependent excited-state lifetime of phenol under the S_1/S_2 conical intersection. *J. Chem. Phys.* **149**, 031104. (doi:10.1063/1.5041992)
48. Woo KC, Kim SK. 2019 Multidimensional H atom tunneling dynamics of phenol: interplay between vibrations and tunneling. *J. Phys. Chem. A* **123**, 1529–1537. (doi:10.1021/acs.jpca.9b00327)
49. Nix MGD, Devine AL, Cronin B, Dixon RN, Ashfold MNR. 2006 High resolution photofragment translational spectroscopy studies of the near ultraviolet photolysis of phenol. *J. Chem. Phys.* **125**, 133318. (doi:10.1063/1.2353818)
50. Dixon RN, Oliver TAA, Ashfold MNR. 2011 Tunnelling under a conical intersection: application to the product vibrational state distributions in the UV photodissociation of phenols. *J. Chem. Phys.* **134**, 194303. (doi:10.1063/1.3585609)
51. Xie CJ, Zhao B, Malbon C, Yarkony DR, Xie DQ, Guo H. 2020 Insights into the mechanism of nonadiabatic photodissociation from product vibrational distributions. The remarkable case of phenol. *J. Phys. Chem. Lett.* **11**, 191–198. (doi:10.1021/acs.jpclett.9b03407)
52. Woo KC, Kim J, Kim SK. 2021 Conformer-specific tunneling dynamics dictated by the seam coordinate of the conical intersection. *J. Phys. Chem. Lett.* **12**, 1854–1861. (doi:10.1021/acs.jpclett.0c03742)
53. Pino GA, Oldani AN, Marceca E, Fujii M, Ishiuchi S-I, Miyazaki M, Broquier M, Dedonder C, Jouvet C. 2010 Excited state hydrogen transfer dynamics in substituted phenols and their complexes with ammonia: $\pi\pi^*$-$\pi\sigma^*$ energy gap propensity and ortho-substitution effect. *J. Chem. Phys.* **133**, 124313. (doi:10.1063/1.3480396)
54. King GA, Devine AL, Nix MGD, Kelly DE, Ashfold MNR. 2008 Near-UV photolysis of substituted phenols. Part II. 4-, 3- and 2-methylphenol. 2008. *Phys. Chem. Chem. Phys.* **10**, 6417–6429. (doi:10.1039/b809250h)
55. Aota T, Ebata T, Ito M. 1989 Rotational isomers and internal rotation of the methyl group in S_0, S_1 and ion of o-cresol. *J. Phys. Chem.* **93**, 3519–3522. (doi:10.1021/j100346a031)
56. Ashfold MNR, Cronin B, Devine AL, Dixon RN, Nix MGD. 2006 The role of $\pi\sigma^*$ excited states in the photodissociation of heteroaromatic molecules. *Science* **312**, 1637–1640. (doi:10.1126/science.1125436)
57. Ashfold MNR, King GA, Murdock D, Nix MGD, Oliver TAA, Sage AG. 2010 $\pi\sigma^*$ excited states in molecular photochemistry. *Phys. Chem. Chem. Phys.* **12**, 1218–1238. (doi:10.1039/b921706a)
58. You HS, Han S, Yoon JH, Lim JS, Lee J, Kim SY, Ahn DS, Lim JS, Kim SK. 2015 Structure and dynamic role of conical intersections in the pi sigma*-mediated photodissociation reactions. *Int. Rev. Phys. Chem.* **34**, 429–459. (doi:10.1080/0144235X.2015.1072364)
59. King GA, Oliver TAA, Dixon RN, Ashfold MNR. 2012 Vibrational energy redistribution in catechol during ultraviolet photolysis. *Phys. Chem. Chem. Phys.* **14**, 3338–3345. (doi:10.1039/c2cp22642a)
60. Weiler M, Miyazaki M, Feraud G, Ishiuchi S, Dedonder C, Jouvet C, Fujii M. 2013 Unusual behavior in the first excited state lifetime of catechol. *J. Phys. Chem. Lett.* **4**, 3819–3823. (doi:10.1021/jz402089m)
61. Devine AL, Nix MGD, Dixon RN, Ashfold MNR. 2008 Near ultraviolet photodissociation of thiophenol. *J. Phys. Chem. A* **112**, 9563–9574. (doi:10.1021/jp802019v)
62. Marchetti B, Karsili TNV, Cipriani M, Hansen CS, Ashfold MNR. 2017 The near ultraviolet photodissociation dynamics of 2- and 3-substituted thiophenols: geometric vs. electronic structure effects. *J. Chem. Phys.* **147**, 013923. (doi:10.1063/1.4980035)
63. Woo KC, Kim SK. 2020 Real-time tunneling dynamics through adiabatic potential energy surfaces shaped by a conical intersection. *J. Phys. Chem. Lett.* **11**, 6730–6736. (doi:10.1021/acs.jpclett.0c01892)
64. Vieuxmaire OPJ, Lan Z, Sobolewski AL, Domcke W. 2008 Ab initio characterization of the conical intersections involved in the photochemistry of phenol. *J. Chem. Phys.* **129**, 224307. (doi:10.1063/1.3028049)
65. Venkatesan TS, Ramesh SG, Lan Z, Domcke W. 2012 Theoretical analysis of photoinduced H-atom elimination in thiophenol. *J. Chem. Phys.* **136**, 174312. (doi:10.1063/1.4709608)

66. Xu XF, Zheng JJ, Yang KR, Truhlar DG. 2014 Photodissociation dynamics of phenol: multistate trajectory simulations including tunnelling. *J. Am. Chem. Soc.* **136**, 16 378–16 386. (doi:10.1021/ja509016a)
67. Zhang LY, Truhlar DG, Sun SZ. 2019 Full-dimensional three-state potential energy surfaces and state couplings for photodissociation of thiophenol. *J. Chem. Phys.* **151**, 154306. (doi:10.1063/1.5124870)
68. Hadden DJ, Williams CA, Roberts GM, Stavros VG. 2011 Time-resolved velocity map imaging of methyl elimination from photoexcited anisole. *Phys. Chem. Chem. Phys.* **13**, 4494–4499. (doi:10.1039/c0cp02429e)
69. Lim JS, Kim SK. 2010 Experimental probing of conical intersection dynamics in the photodissociation of thioanisole. *Nat. Chem.* **2**, 627–632. (doi:10.1038/NCHEM.702)
70. Wenge AM, Karsili TNV, Rodriguez JD, Cotterell MI, Marchetti B, Dixon RN, Ashfold MNR. 2015 Tuning photochemistry: substituent effects on $\pi\sigma^*$ state mediated bond fission in thioanisoles. *Phys. Chem. Chem. Phys.* **17**, 16 246–16 256. (doi:10.1039/c5cp01660f)
71. Woo KC, Kang DH, Kim SK. 2017 Real-time observation of nonadiabatic bifurcation dynamics at a conical intersection. *J. Am. Chem. Soc.* **139**, 17 152–17 158. (doi:10.1021/jacs.7b09677)
72. Nix MGD, Devine AL, Dixon RN, Ashfold MNR. 2008 Observation of geometric phase effect induced photodissociation dynamics in phenol. *Chem. Phys. Lett.* **463**, 305–308. (doi:10.1016/j.cplett.2008.08.085)
73. Xie C, Ma J, Zhu X, Yarkony DR, Xie D, Guo H. 2016 Nonadiabatic tunneling in photodissociation of phenol. *J. Am. Chem. Soc.* **138**, 7828–7831. (doi:10.1021/jacs.6b03288)
74. Xie C, Guo H. 2017 Photodissociation of phenol via nonadiabatic tunneling: comparison of two ab initio based potential energy surfaces. *Chem. Phys. Lett.* **683**, 222–227. (doi:10.1016/j.cplett.2017.02.026)
75. Oliver TAA, Zhang Y, Roy A, Ashfold MNR, Bradforth SE. 2015 Exploring autoionization and photo-induced proton-coupled electron transfer pathways of phenol in aqueous solution. *J. Phys. Chem. Lett.* **6**, 4159–4164. (doi:10.1021/acs.jpclett.5b01861)
76. Kusaka R, Nihonyanagi S, Tahara T. 2021 The photochemical reaction of phenol becomes ultrafast at the air–water interface. *Nat. Chem.* **13**, 306–311. (doi:10.1038/s41557-020-00619-5)
77. Mota R *et al.* 2005 Water VUV electronic state spectroscopy by synchrotron radiation. *Chem. Phys. Lett.* **416**, 152–159. (doi:10.1016/j.cplett.2005.09.073)
78. Andresen P, Ondrey GS, Titze B. 1983 Creation of population inversions in the Lambda-doublets of OH by the photo-dissociation of H_2O at 157 nm - a possible mechanism for the astronomical maser. *Phys. Rev. Lett.* **50**, 486–488. (doi:10.1103/PhysRevLett.50.486)
79. Plusquellic DF, Votava O, Nesbitt DJ. 1998 Bond-selective photofragmentation of jet-cooled HOD at 193 nm: vibrationally mediated photochemistry with zero-point excitation. *J. Chem. Phys.* **109**, 6631–6640. (doi:10.1063/1.477314)
80. Yang XF, Hwang DW, Lin JJ, Yang XM. 2000 Dissociation dynamics of the water molecule on the $\tilde{A}^1B_1$ electronic surface. *J. Chem. Phys.* **113**, 10 597–10 604. (doi:10.1063/1.1285899)
81. Lu IC, Wang FY, Yuan KJ, Cheng Y, Yang XM. 2008 Nonstatistical spin dynamics in photodissociation of H_2O at 157 nm. *J. Chem. Phys.* **128**, 066101. (doi:10.1063/1.2830710)
82. Mordaunt DH, Ashfold MNR, Dixon RN. 1994 Dissociation dynamics of H_2O (D_2O) following photoexcitation at the Lyman-alpha wavelength (121.6 nm). *J. Chem. Phys.* **100**, 7360–7375. (doi:10.1063/1.466880)
83. Vondirke M, Heumann B, Kuhl K, Schroder T, Schinke R. 1994 Fluctuations in absorption spectra and final product state distributions following photodissociation processes. *J. Chem. Phys.* **101**, 2051–2068. (doi:10.1063/1.467713)
84. van Harrevelt R, van Hemert MC. 2000 Photodissociation of water. I. Electronic structure calculations for the excited states. *J. Chem. Phys.* **112**, 5777–5786. (doi:10.1063/1.481153)
85. van Harrevelt R, van Hemert MC. 2000 Photodissociation of water. II. Wave packet calculations for the photofragmentation of H_2O and D_2O in the B band. *J. Chem. Phys.* **112**, 5787–5808. (doi:10.1063/1.481154)
86. Cheng YA, Yuan KJ, Cheng LN, Guo Q, Dai DX, Yang XM. 2011 Photodissociation dynamics of H_2O: effect of unstable resonances on the $\tilde{B}^1A_1$ electronic state. *J. Chem. Phys.* **134**, 064301. (doi:10.1063/1.3554213)

87. Zhou LS, Jiang B, Xie DQ, Guo H. 2013 State-to-state photodissociation dynamics of H_2O in the B-band: competition between two coexisting nonadiabatic pathways. *J. Phys. Chem. A* **117**, 6940–6947. (doi:10.1021/jp310546g)
88. Yuan KJ, Dixon RN, Yang XM. 2011 Photochemistry of the water molecule: adiabatic versus nonadiabatic dynamics. *Acc. Chem. Res.* **44**, 369–378. (doi:10.1021/ar100153g)
89. Bin J, Xie DQ, Guo H. 2012 State-to-state photodissociation dynamics of triatomic molecules: H_2O in the B band. *J. Chem. Phys.* **136**, 304302. (doi:10.1063/1.3676725)
90. Harich SA, Yang XF, Yang XM, van Harrevelt R, van Hemert MC. 2001 Single rotational product propensity in the photodissociation of HOD. *Phys. Rev. Lett.* **87**, 263001. (doi:10.1103/PhysRevLett.87.263001)
91. Dixon RN, Hwang DW, Yang XF, Harich S, Lin JJ, Yang XM. 1999 Chemical 'double slits': dynamical interference of photodissociation pathways in water. *Science* **285**, 1249–1253. (doi:10.1126/science.285.5431.1249)
92. Harich SA, Hwang DW, Yang XF, Lin JJ, Yang XM, Dixon RN. 2000 Photodissociation of H_2O at 121.6 nm: a state-to-state dynamical picture. *J. Chem. Phys.* **113**, 10 073–10 090. (doi:10.1063/1.1322059)
93. Zhou L, Xie DQ, Guo H. 2015 Signatures of non-adiabatic dynamics in the fine-structure state distributions of the OH(X/A) products in the B-band photodissociation of H_2O. *J. Chem. Phys.* **142**, 124317. (doi:10.1063/1.4915536)
94. Fillion JH, Ruiz J, Yang XF, Castillejo M, Rostas F, Lemaire JL. 2004 High resolution photoabsorption and photofragment fluorescence spectroscopy of water between 10.9 and 12 eV. *J. Chem. Phys.* **120**, 6531–6541. (doi:10.1063/1.1652566)
95. Ashfold MNR, Bayley JM, Dixon RN. 1984 Molecular predissociation dynamics revealed through multiphoton ionisation spectroscopy, I: the $\tilde{C}^1B_1$ states of H_2O and D_2O. *Chem. Phys.* **84**, 35–50. (doi:10.1016/0301-0104(84)80004-X)
96. Yuan KJ, Cheng Y, Cheng L, Guo Q, Dai DX, Wang XY, Yang XM, Dixon RN. 2008 Nonadiabatic dissociation dynamics in H_2O: competition between rotationally and nonrotationally mediated pathways. *Proc. Nat Acad. Sci. USA* **105**, 19 148–19 153. (doi:10.1073/pnas.0807719105)
97. Dixon RN, Oliver TAA, Cheng L, Cheng Y, Yuan KJ, Xang XM. 2013 Vibronically induced decay paths from the $\tilde{C}^1B_1$ state of water and its isotopomers. *J. Chem. Phys.* **138**, 104306. (doi:10.1063/1.4794158)
98. He ZG, Yang DY, Chen CZ, Yuan KJ, Dai DX, Wu GR, Yang XM. 2017 An accidental resonance mediated predissociation pathway of water molecules excited to the electronic $\tilde{C}$ state. *Phys. Chem. Chem. Phys.* **19**, 29 795–29 800. (doi:10.1039/c7cp06286a)
99. Chang Y, Chen ZC, Zhou JM, Luo ZJ, He ZG, Wu GR, Ashfold MNR, Yuan KJ, Yang XM. 2019 Striking isotopologue-dependent photodissociation dynamics of water molecules: the signature of an accidental resonance. *J. Phys. Chem. Lett.* **10**, 4209–4214. (doi:10.1021/acs.jpclett.9b01710)
100. Chang Y *et al.* 2019 Hydroxyl super rotors from vacuum ultraviolet photodissociation of water. *Nat. Commun.* **10**, 1250. (doi:10.1038/s41467-019-09176-z)
101. Chang Y *et al.* 2020 Water photolysis and its contributions to the hydroxyl dayglow emissions in the atmospheres of Earth and Mars. *J. Phys. Chem. Lett.* **11**, 9086–9092. (doi:10.1021/acs.jpclett.0c02803)
102. Sussmann BJ, Townsend D, Ivanov MY, Stolow A. 2006 Dynamic Stark control of photochemical processes. *Science* **314**, 278–281. (doi:10.1126/science.1132289)
103. Corrales ME, Gonzalez-Vazquez J, Balerdi G, Sola IR, de Nalda R, Banares L. 2014 Control of ultrafast molecular photodissociation by laser-field-induced potentials. *Nat. Chem.* **6**, 785–790. (doi:10.1038/nchem.2006)
104. Hilsabeck KI, Meiser JL, Sneha M, Harrison JA, Zare RN. 2019 Nonresonant photons catalyze photodissociation of phenol. *J. Am. Chem. Soc.* **141**, 1067–1073. (doi:10.1021/jacs.8b11695)
105. Van den Berg JL, Neumann KI, Harrison JA, Weir H, Hohenstein EG, Martinez TJ, Zare RN. 2020 Strong, nonresonant radiation enhances cis-trans photoisomerization of stilbene in solution. *J. Phys. Chem. A* **124**, 5999–6008. (doi:10.1021/acs.jpca.0c02732)
106. Wrede E, Laubach S, Schulenburg S, Brown A, Wouters ER, Orr-Ewing AJ, Ashfold MNR. 2001 Continuum state spectroscopy: a high resolution ion imaging study of IBr photolysis in the wavelength range 440–685 nm. *J. Chem. Phys.* **114**, 2629–2646. (doi:10.1063/1.1337049)

107. Eppink ATJB, Parker DH. 1999 Energy partitioning following photodissociation of methyl iodide in the A band: a velocity mapping study. *J. Chem. Phys.* **110**, 832–844. (doi:10.1063/1.478051)
108. Kobayashi Y, Chang KF, Zeng T, Neumark DM, Leone SR. 2019 Direct mapping of curve-crossing dynamics in IBr by attosecond transient absorption spectroscopy. *Science* **365**, 79–83. (doi:10.1126/science.aax0076)
109. Murillo-Sanchez ML, Gonzalez-Vazquez J, Corrales ME, de Nalda R, Martinez-Nunez E, Garcia-Vela A, Banares L. 2020 Femtochemistry under scrutiny: clocking state-resolved channels in the photodissociation of CH_3I in the A-band. *J. Chem. Phys.* **152**, 014304. (doi:10.1063/1.5134473)
110. Chang KF, Wang H, Poullain SM, Prendergast D, Neumark DM, Leone SR. 2021 Mapping wave packet bifurcation at a conical intersection in CH_3I by attosecond XUV transient absorption spectroscopy. *J. Chem. Phys.* **154**, 234301. (doi:10.1063/5.0056299)
111. Wang H, Odelius M, Prendergast D. 2019 A combined multi-reference pump-probe simulation method with application to XUV signatures of ultrafast methyl iodide photodissociation. *J. Chem. Phys.* **151**, 124106. (doi:10.1063/1.5116816)
112. Keefer D, Aleotti F, Rouxel JR, Segatta F, Gu B, Nenov A, Garavelli M, Mukamel S. 2021 Imaging conical intersection dynamics during azobenzene photoisomerization by ultrafast X-ray diffraction. *Proc. Nat Acad. Sci. USA* **118**, e2022037118. (doi:10.1073/pnas.2022037118)
113. Cavaletto SM, Keefer D, Rouxel JR, Aleotti F, Segatta F, Garavelli M, Mukamel S. 2021 Unveiling the spatial distribution of molecular coherences at conical intersections by covariance X-ray diffraction signals. *Proc. Nat Acad. Sci. USA* **118**, e2105046118. (doi:10.1073/pnas.2105046118)